Journal of Communication Engineering (JCE)

P- ISSN: 2322-4088 Vol. 12, No. 1, Jan.-Jun. 2023 E- ISSN: 2322-3936

Introducing a Method-of-Moments Solution for 2-Dimensional TM Electromagnetic Problems

M. Parizi Electrical Engineering Dept.; Yazd University; Yazd, Iran;
Email: mahdi.parizi@stu.yazd.ac.ir

M. Nakhkash* **[Corresponding Author]** Electrical Engineering Dept.; Yazd University; Yazd, Iran;
Email: nakhkash@yazd.ac.ir

Received: *06 Jan. 2023* ***Revised:*** *29 Mar. 2023* ***Accepted:*** *25 Apr. 2023*

Abstract: This paper introduces a new solution for 2-dimensional (2D) TM electromagnetic problems by the method of moments (MoM) in polar coordinates. The main idea is to reformulate a 2D problem according to addition theorem for the zeroth-order Hankel function of the second kind. Recursive formulas in spatial frequency domain are derived and the scattering field is rewritten into inward and outward components. In this way, a 2D TM problem can be solved using 1D FFT in the stabilized biconjugate-gradient fast Fourier transform (BCGS-FFT) algorithm. Because the emerging method obtains 1D FFT over a circle, there is no need to expand an object region by zero padding, whereas it is necessary for the conventional 2D FFT in cartesian coordinates. Therefore, the polar coordinate approach concludes in less computational burden. Other interesting advantage is that the field on a circle outside a scattering object can be calculated, efficiently, using an analytical formula. This is, particularly, attractive in electromagnetic inverse scattering problems and microwave imaging (MI). The numerical examples for 2D TM problems demonstrate merits of the proposed technique in terms of the accuracy and computational efficiency.

Index Terms: 2-Dimensional TM Problem, Method of Moments (MoM), Stabilized Biconjugate-gradient Fast Fourier Transform, Microwave Imaging.

Citation: M. Parizi and M. Nakhkash, "Introducing a Method-of-Moments Solution for 2-Dimensional TM Electromagnetic Problems," *Journal of Communication Engineering*, vol. 12, no. 1, pp. 47-66, Jan.-Jun. 2023.
http://dx.doi.org/10.22070/jce.2025.19053.1269

I. INTRODUCTION

There exist a number of algorithms to numerically obtain electromagnetic fields from Maxwell's equations, among them are full-wave methods [1, 2]. Such methods are iterative-oriented and each iteration involves the computation of integro-difference equations. The most widely used full-wave methods are the MoM [3], the finite element method (FEM) [4], and the finite- difference time-domain (FDTD) method [5]. Our focus in this paper is on developing an efficient MoM to solve 2D TM scattering problems that can be employed in microwave imaging.

Richmond is the first person who provide MoM solutions to 2-dimensional TM [6] and TE [7] problems in order to obtain the scattered wave from a dielectric object. The MoM results in a system of linear equations with many unknowns, whose solution is computationally intensive. Having stability against numerical error, the conjugate gradient (CG) method is an appropriate iterative procedure to solve a system of linear equations. The CG needs a matrix-vector product (MVP) in each iteration and $O(N^2)$ arithmetic multiplications is required for each MVP, where N is the number of unknowns. However, the convolutional nature of the electric field integral equation (EFIE) makes efficient implementation of the MVP using the FFT. The computational cost is, therefore, reduced to $O(N \log_2 N)$ and the CG becomes an efficient algorithm. Van Den Berg [8] and Sarkar [9] employ the conjugate gradient fast Fourier transform (CG-FFT) technique, in which the CG uses the FFT technique to perform the required MVP operations in each iteration. Su [10] solves a 2D TE problem applying CG-FFT to MoM with pulse function expansion and point matching. It was observed that pulse function expansion and point matching did not provide enough accuracy for TE problems [11] and Zwamborn and Van Den Berg overcame this difficulty by introducing the weak form of CG-FFT for TE problems [12]. Some efforts are, also, made to improve the speed and convergence of the CGFFT [13].

In continuation of CG-FFT, the biconjugate gradient FFT (BCG-FFT) method shows promising speed of convergency in comparison with CG-FFT [14, 15]; however, in some special cases, BCG-FFT becomes useless and it is necessary to stabilize the answer of the algorithm in each iteration. Hence, avoiding the calculation of adjoint matrix, the stabilized version of BCG-FFT, i.e. BCGS-FFT, provides more speed and simplicity than CG-FFT and BCG-FFT in different MI applications [16-18]. There are many papers, which have dealt with the MoM solution of the EFIE and the state-of-art ones can be found in [19].

Authors in [20] introduce a technique in cartesian coordinates to use 1D FFT instead of 2D FFT to solve 2D electromagnetic problems. The idea is to decompose Green's function of 2D homogeneous media and rewrite scattering fields into upward and downward components. In this way, the 1D FFT instead of the 2D one is employed to solve the 2D EFIE. Although such an idea

owns some merits, it provides no significant improvement over the use of the 2D FFT. Proceeding the same approach, this paper extends the idea to polar coordinates. According to addition theorem for the zeroth-order Hankel function of the second kind in polar system, we attempt to solve 2D TM problems using 1D FFT by rewriting the scattering field into inward and outward components. We derive new recursive formulas, in which the pre-computations can be capsulated, and solve a 2D TM problem using 1D FFT in BCGS-FFT algorithm. Obtaining 1D FFT over a circle, there is no need for zero-padding and together with the use of pre-computations, the method saves considerable memory and time over the conventional approach. The same approach is taken in [21] to formulate TE and TM scattering problems for 2D conducting structures, whereas our approach is for 2D dielectric penetrable objects. Other interesting advantage of our approach is that the field on a circle outside a scattering object can be calculated, efficiently, using an analytical formula. This is, particularly, attractive in electromagnetic inverse scattering problems and microwave imaging.

Let denote 2Dfft-MoM for the conventional approach and 1Dfft-MoM for our approach. The novelty of the 1Dfft-MoM can be summarized as follows:

a) In the 1Dfft-MoM, we obtain 1D FFT over a circle, which is periodic and, hence, there is no need for zero-padding, improving the computational efficiency. Several numerical examples indicate the computational cost for the 1Dfft-MoM is lower than that for the 2Dfft-MoM. Moreover, the 1Dfft-MoM needs less storage and its accuracy is comparable to that of the 2Dfft-MoM.
b) After calculating the electric field inside the object region by the 2Dfft-MoM, the EFIE is, numerically, computed to obtain the field at any point outside the object region. That means the calculation of the electric field at any point outside the object region needs N complex multiplications, where N is the number of cells in the object region. However, with the aid of an analytical formula in the 1Dfft-MoM, the computational cost for one point is, nearly, on order of $\log_2(4\sqrt{N})$. Thus, the computational efficiency is, significantly, improved in the calculation of the electric field outside the object region.

A state-of-art work [22] employs a deep neural network to solve 2D TM problems. Authors in [22] discretize the object domain in cartesian coordinates and solve the emerging linear equations by a trained multilayer neural network (TMNW). The number of layers is equal to the number of iterations and the solution at an iteration is the output of the corresponding layer of the TMNW. The inputs to each layer need the MVP that is obtained by the 2D FFT and therefore, the 2D zeros-padding is required.

In the algorithm of [22], one can employ our approach, i.e. one can discretize the object region in polar coordinates and solve 2D TM problems by a TMNW. The MVP in each layer of the TMNW can be obtained by the use of 1D FFT. Thus, the use of our proposal in TMNW would improve the efficiency and accuracy in comparison to the use of the conventional 2D FFT.

It should be emphasized both 1Dfft-MoM and 2Dfft-MoM can employ the CG, BCG, BCGS or even TMNW to converge to the exact solution of a 2D TM problem. All four algorithms (CG, BCG, BCGS and TMNW) need the MVP in their iterations. The MVP is the numerical realization of the electric field integral equation with a given total electric field inside the object region. The 2Dfft-MoM evaluates the MVP in cartesian coordinates with 2D FFT, whereas 1Dfft-MoM performs the MVP in polar coordinates with aid of our recursive formula and the 1D FFT.

II. 2D ELECTROMAGNETIC PROBLEM

Consider the geometry of a 2D electromagnetic scattering problem shown in Fig. 1, where an inhomogeneous object with spatial support of D is located in a background medium with the permittivity ε_b, conductivity σ_b and permeability μ_b. The object has the spatially variable permittivity $\varepsilon(\mathbf{r})$, conductivity $\sigma(\mathbf{r})$, where $\mathbf{r}=x\,\hat{x}+y\,\hat{y}$, and a constant permeability $\mu=\mu_b$ (i.e. the object and the background medium are nonmagnetic). For TMz problems, the total electric field satisfies

$$E_z(\mathbf{r})=E_z^i(\mathbf{r})+E_z^s(\mathbf{r})=E_z^i(\mathbf{r})+k_b^2 A_z(\mathbf{r}) \tag{1}$$

where $E_z(\mathbf{r})$, $E_z^i(\mathbf{r})$ and $E_z^s(\mathbf{r})$ are, respectively, z components of the total, incident and scattered fields. The vector potential $A_z(\mathbf{r})$ is equal to

$$A_z(\mathbf{r})=\iint_D g(\mathbf{r},\mathbf{r}')\,\psi_z(\mathbf{r}')\,d^2\mathbf{r}',\ \psi_z(\mathbf{r})=\chi(\mathbf{r})E_z(\mathbf{r}) \tag{2}$$

in which $g(\mathbf{r}),\psi_z(\mathbf{r})$ and $\chi(\mathbf{r})$ are scalar Green's function of the background medium, the induced source and the object function respectively. With a time dependency of $e^{j\omega t}$, $\chi(\mathbf{r})=k^2(\mathbf{r})/k_b^2-1$ where $k_b^2=\omega^2\mu_b\varepsilon_b-j\omega\mu_b\sigma_b$ and $k^2(\mathbf{r})=\omega^2\mu_b\varepsilon(\mathbf{r})-\omega\mu_b\sigma(\mathbf{r})$.

In order to solve (1), the iterative algorithms need the computation of (2) for known $\psi_z(\mathbf{r})$ at every iteration. Let the object domain D be embedded in a rectangle region $\Re$ that is discretized to $M_x\times N_y$ square cells, where M_x and N_y are the discretization numbers in x and y directions respectively. Selecting the proper testing and expansion functions and obtaining (2) by the MoM, Eq. (2) is converted to MVP, whose direct evaluation requires $O(N^2)$, where $N=M_x\times N_y$, arithmetic operations. However, the convolutional form of (2) suggests the use of 2D FFT to reduce the computational cost. Denoting $a_z(m,n)$ and $\phi_z(m,n)$ the coefficients of the discrete

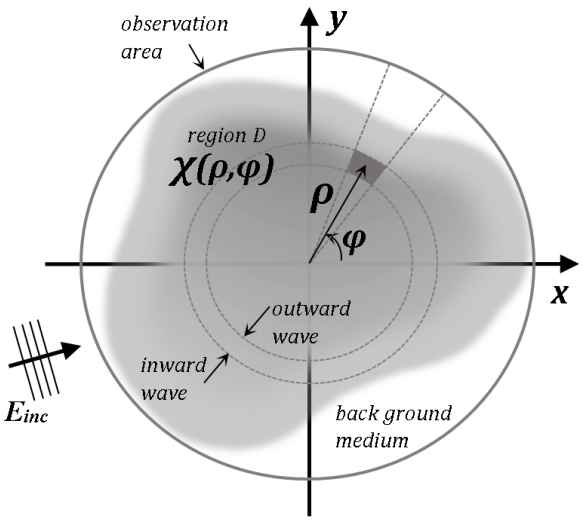

Fig. 1. The geometry of a 2D electromagnetic problem and it's discretization along ρ and φ in polar coordinates

version of $A_z(\mathbf{r})$ and $\psi_z(\mathbf{r})$, respectively, $a_z(m,n)$ can be written as [19, 23]

$$a_z(m,n)=\mathrm{FFT}^{-1}\left\{\mathrm{FFT}\left[g(m,n)\right]\mathrm{FFT}\left[\phi_z(m,n)\right]\right\} \tag{3}$$

where $g(m,n)$ is, approximately, obtained by integrating $g(\mathbf{r})$ over circle cells, whose surfaces are equivalent to the square cells. It is necessary to expand embedding region $\Re$ with at least M_x and N_y cells in x and y directions, respectively, so as to correctly calculate $A_z(\mathbf{r})$ using the FFT. Therefore, $g(m,n)$ and $\phi_z(m,n)$ will have $2M_x \times 2N_y$ elements (i.e. $g(m,n)$ and $\phi_z(m,n)$ are zero-padded). Consequently, the total number of complex multiplications for evaluating the discrete version of Eq. (2) with a given total electric field inside the embedding region would be

$$N_{\mathrm{2DFFT}}=8M_x N_y \log_2(4M_x N_y)+8M_x N_y \tag{4}$$

where the second term at the right side of (4) accounts for the multiplication inside the curve brackets ({}) in (1) and obtaining the induced source $\phi_z(m,n)$ (Eq. (2)). The dominant factor that determines the computational cost is the first right term of (4). We refer to the conventional method as 2Dfft-MoM throughout the paper.

III. SPLITTING VECTOR POTENTIAL IN POLAR COORDINATE

The Green's function for 2D problems can be written as [24]

$$g(\mathbf{r},\mathbf{r}')=-\frac{j}{4}H_0^{(2)}(k_b\left|\mathbf{r}-\mathbf{r}'\right|) \tag{5}$$

in which $H_0^{(2)}$ is zeroth-order Hankel function of the second kind. Inserting (5) into (2), the resultant relation in polar coordinate is given by

$$A_z(\rho,\varphi)=\frac{-j}{4}\iint_D H_0^{(2)}(k_b|\mathbf{r}-\mathbf{r}'|)\,\psi_z(\rho',\varphi')\,\rho' d\rho' d\varphi' \,, \tag{6}$$
$$|\mathbf{r}-\mathbf{r}'|=\sqrt{\rho^2+\rho'^2-2\rho\rho'\cos(\varphi-\varphi')}$$

The addition theorem for the Hankel function provides [24]

$$H_0^{(2)}(k_b|\mathbf{r}-\mathbf{r}'|)=\begin{cases}\sum_{n=-\infty}^{\infty} H_n^{(2)}(k_b\rho)J_n(k_b\rho')\ \mathrm{e}^{jn(\phi-\phi')}, & \rho'\le\rho\\ \sum_{n=-\infty}^{\infty} J_n(k_b\rho)\ H_n^{(2)}(k_b\rho')\,\mathrm{e}^{jn(\phi-\phi')}, & \rho'>\rho\end{cases} \tag{7}$$

where $H_n^{(2)}$ and J_n are nth-order Hankel function of the second kind and nth-order Bessel function, respectively. Considering the circle C in Fig. 1 is within region D, one can decompose $A_z(\rho,\varphi)$ on this circle to outward and inward waves $A_z^{\text{out}}(\rho,\varphi)$ and $A_z^{\text{in}}(\rho,\varphi)$. Hence, we have

$$A_z^{\text{out}}(\rho,\varphi)=\frac{-j}{4}\sum_{n=-\infty}^{\infty} H_n^{(2)}(k_b\rho)\mathrm{e}^{jn\varphi}\iint_{D_{\text{out}}} J_n(k_b\rho')\psi_z(\rho',\varphi')\mathrm{e}^{-jn\varphi'}\rho' d\rho' d\varphi' \tag{8}$$

where $D_{\text{out}}=\{(\rho',\varphi')\in D\,|\,\rho'\le\rho\}$. In the same way, we have

$$A_z^{\text{in}}(\rho,\varphi)=\frac{-j}{4}\sum_{n=-\infty}^{\infty} J_n(k_b\rho)\mathrm{e}^{jn\varphi}\iint_{D_{\text{in}}} H_n^{(2)}(k_b\rho')\psi_z(\rho',\varphi')\mathrm{e}^{-jn\varphi'}\rho' d\rho' d\varphi' \tag{9}$$

in which $D_{\text{in}}=\{(\rho',\varphi')\in D\,|\,\rho'>\rho\}$. The outward and inward waves are periodic in terms of angle φ. The outward wave in form of Fourier series is

$$A_z^{\text{out}}(\rho,\varphi)=\sum_{n=-\infty}^{\infty}\tilde{A}_z^{\text{out}}(\rho,n)\ \mathrm{e}^{jn\varphi}\ ,\ \tilde{A}_z^{\text{out}}(\rho,n)=\frac{-j}{4}H_n^{(2)}(k_b\rho)\,I_n^{\text{out}} \tag{10}$$

$$I_n^{\text{out}}=\iint_{D_{\text{out}}} J_n(k_b\rho')\psi_z(\rho',\varphi')\,\mathrm{e}^{-jn\varphi'}\,\rho' d\rho' d\varphi' \tag{11}$$
$$=2\pi\int_0^{\rho}\rho' J_n(k_b\rho')\left[\frac{1}{2\pi}\int_0^{2\pi}\psi_z(\rho',\varphi')\,\mathrm{e}^{-jn\varphi'}d\varphi'\right]d\rho'$$

The integral term in the bracket in (11) is the Fourier series coefficients of $\psi_z(\rho',\varphi')$ in terms of φ'. Denoting $\tilde{\psi}_z(\rho',n)=\frac{1}{2\pi}\int_0^{2\pi}\psi_z(\rho',\varphi')\mathrm{e}^{-jn\varphi'}d\varphi'$, we have

$$\tilde{A}_z^{\text{out}}(\rho,n)=\frac{-j\pi}{2}H_n^{(2)}(k_b\rho)\int_0^{\rho}\rho' J_n(k_b\rho')\tilde{\psi}_z(\rho',n)\,d\rho' \tag{12}$$

Considering the embedding region $\Re$, herein, is a circle surface that includes the object region D and has radius a, in the same way, one can derive

$$A_z^{\text{in}}(\rho,\varphi)=\sum_{n=-\infty}^{\infty}\tilde{A}_z^{\text{in}}(\rho,n)\,\mathrm{e}^{j\,n\,\varphi} \tag{13}$$

$$\tilde{A}_z^{\text{in}}(\rho,n)=\frac{-j\,\pi}{2}J_n(k_b\,\rho)\int_{\rho}^{a}\rho' H_n^{(2)}(k_b\,\rho')\tilde{\psi}_z(\rho',n)\,d\,\rho'$$

Let the embedding region be discretized to M_ρ rings in ρ direction, each having the thickness $\Delta_1,\Delta_2,...,\Delta_{M_\rho}$ starting from the origin. Also, let define $\rho_0=0$, $\rho_L=\sum_{m=1}^{L}\Delta_m$ as the edge rings and $\rho_{i-1/2}=\rho_i-\Delta_i/2$, $1\le i\le M_\rho$ as the middle rings. One can rewrite the Fourier coefficients of outward wave in Eq. (12) at $\rho_{L-1/2}$ as

$$\tilde{A}_z^{\text{out}}(\rho_{L-1/2},n)=\frac{-j\,\pi}{2}H_n^{(2)}(k_b\,\rho_{L-1/2})\left[\begin{array}{l}\displaystyle\sum_{m=1}^{L-1}\int_{\rho_{m-1}}^{\rho_m}\rho' J_n(k_b\,\rho')\,\tilde{\psi}_z(\rho',n)\,d\,\rho' \\ \displaystyle+\int_{\rho_{L-1}}^{\rho_{L-1/2}}\rho' J_n(k_b\,\rho')\,\tilde{\psi}_z(\rho',n)\,d\,\rho'\end{array}\right] \tag{14}$$

If Δ_m s are enough small, the induced field does not vary, significantly, in interval $[\rho_{m-1},\rho_m]$ and we may use the approximation $\tilde{\psi}_z(\rho',n)=\tilde{\psi}_z(\rho_{m-1}+\Delta_m/2,n)=\tilde{\psi}_z(\rho_{m-1/2},n)$, i.e. the basis function is chosen as pulse function in ρ direction. Substitution of this approximation in (14) yields:

$$\tilde{A}_z^{\text{out}}(\rho_{L-1/2},n)\;\square\;\frac{-j\,\pi}{2}H_n^{(2)}(k_b\,\rho_{L-1/2})\left[\begin{array}{l}\displaystyle\sum_{m=1}^{L-1}\tilde{\psi}_z(\rho_{m-1/2},n)\int_{\rho_{m-1}}^{\rho_m}\rho' J_n(k_b\,\rho')\,d\,\rho' \\ \displaystyle+\tilde{\psi}_z(\rho_{L-1/2},n)\int_{\rho_{L-1}}^{\rho_{L-1/2}}\rho' J_n(k_b\,\rho')\,d\,\rho'\end{array}\right] \tag{15}$$

The only term in(15), which is a function of electrical field, is $\tilde{\psi}_z(\rho_{m-1/2},n)$. Let introduce the definition

$$\tilde{B}_z^{\text{out}}(\rho_L,n)=\sum_{m=1}^{L}\tilde{\psi}_z(\rho_{m-1/2},n)\int_{\rho_{m-1}}^{\rho_m}\rho' J_n(k_b\,\rho')d\,\rho' \tag{16}$$

Then, (15) is given by

$$\tilde{A}_z^{\text{out}}(\rho_{L-1/2},n)=\frac{-j\,\pi}{2}H_n^{(2)}(k_b\,\rho_{L-1/2})\tilde{B}_z^{\text{out}}(\rho_{L-1/2},n) \tag{17}$$

Eqs. (15) and (16) suggests a recursive formula as

$$\tilde{B}_z^{\text{out}}(\rho_{L-1/2},n)=\tilde{B}_z^{\text{out}}(\rho_{L-1},n)+\tilde{\psi}_z(\rho_{L-1/2},n)\int_{\rho_{L-1}}^{\rho_{L-1/2}}\rho' J_n(k_b\rho')d\rho' \tag{18}$$

$$\tilde{B}_z^{\text{out}}(\rho_L,n)=\tilde{B}_z^{\text{out}}(\rho_{L-1},n)+\tilde{\psi}_z(\rho_{L-1/2},n)\int_{\rho_{L-1}}^{\rho_L}\rho' J_n(k_b\rho')d\rho'$$

Hence, to obtain $\tilde{B}_z^{\text{out}}$, it is enough to compute an integral term and use this integral in the second right term of (18) and add to $\tilde{B}_z^{\text{out}}$ for the preceding ring. The integral term is independent of the object and, totally, depends on the background parameters. Consequently, this integral for a given background can be pre-computed regardless of the object. In this way, the computational complexity is reduced during the calculation of the scattered field for different objects. Such a situation occurs in microwave imaging of objects.

To implement pre-computation, integral term in (18) could be obtained, recursively, using Bessel equations. In this manner, we have [25]

$$\int_{\rho_{m-1}}^{\rho_m}\rho' J_n(k_b\rho')d\rho'=\frac{2(n-1)}{k_b}\int_{\rho_{m-1}}^{\rho_m}J_{n-1}(k_b\rho')d\rho'-\int_{\rho_{m-1}}^{\rho_m}\rho' J_{n-2}(k_b\rho')d\rho' \tag{19}$$

To solve the first right hand term of (19), the relation (20) is employed

$$\int_{\rho_{m-1}}^{\rho_m}J_n(k_b\rho')d\rho'=\int_{\rho_{m-1}}^{\rho_m}J_{n-2}(k_b\rho')d\rho'-\frac{2}{k_b}J_{n-1}(k_b\rho')\Big|_{\rho_{m-1}}^{\rho_m},\ n>1 \tag{20}$$

In order to proceed with the recursive relations (19) and (20), it is required to obtain the integral of the zeroth and first order Bessel functions, whose detail calculations are given by relation (A3) in Appendix.

For inward wave, if one obtains $\tilde{A}_z^{\text{in}}(\rho,n)$ at the middle of a ring $\rho=\rho_{L-1/2}=\rho_L-\Delta_L/2$, Eq. (13) gives following relations

$$\tilde{B}_z^{\text{in}}(\rho_L,n)=\sum_{m=L+1}^{M}\tilde{\psi}_z(\rho_{m-1/2},n)\int_{\rho_{m-1}}^{\rho_m}\rho' H_n^{(2)}(k_b\rho')d\rho' \tag{21}$$

and

$$\tilde{A}_z^{\text{in}}(\rho_{L-1/2},n)=\frac{-j\pi}{2}J_n(k_b\rho_{L-1/2})\tilde{B}_z^{\text{in}}(\rho_{L-1/2},n) \tag{22}$$

$$\tilde{B}_z^{\text{in}}(\rho_{L-1/2},n)=\tilde{B}_z^{\text{in}}(\rho_L,n)+\tilde{\psi}_z(\rho_{L-1/2},n)\int_{\rho_{L-1/2}}^{\rho_L}\rho' H_n^{(2)}(k_b\rho')d\rho'$$

$$\tilde{B}_z^{\text{in}}(\rho_L,n)=\tilde{B}_z^{\text{in}}(\rho_{L+1},n)+\tilde{\psi}_z(\rho_{L+1/2},n)\int_{\rho_L}^{\rho_{L+1}}\rho' H_n^{(2)}(k_b\rho')d\rho'$$

where the integral terms in (22) can be obtained with the aid of equations

$$\int_{\rho_{m-1}}^{\rho_m} \rho' H_n^{(2)}(k_b \rho')d\rho' = \frac{2(n-1)}{k_b} \int_{\rho_{m-1}}^{\rho_m} H_{n-1}^{(2)}(k_b \rho')d\rho' - \int_{\rho_{m-1}}^{\rho_m} \rho' H_{n-2}^{(2)}(k_b \rho')d\rho' \tag{23}$$

$$\int_{\rho_{m-1}}^{\rho_m} H_{n-1}^{(2)}(k_b \rho')d\rho' = \int_{\rho_{m-1}}^{\rho_m} H_{n-3}^{(2)}(k_b \rho')d\rho' - \frac{2}{k_b} H_{n-2}^{(2)}(k_b \rho')\Big|_{\rho_{m-1}}^{\rho_m} \qquad n > 2$$

Again, the integral of the zeroth and first order functions are given in Appendix.

Now, we can merge $\tilde{B}_z^{\text{out}}(\rho_{L-1/2}, n)$ and $\tilde{B}_z^{\text{in}}(\rho_{L-1/2}, n)$ to obtain $\tilde{A}_z(\rho_{L-1/2}, n)$

$$\begin{aligned} \tilde{A}_z(\rho_{L-1/2}, n) &= \tilde{A}_z^{\text{out}}(\rho_{L-1/2}, n) + \tilde{A}_z^{in}(\rho_{L-1/2}, n) \\ &= \frac{-j\pi}{2} \begin{Bmatrix} H_n^{(2)}(k_b \rho_{L-1/2}) \tilde{B}_z^{\text{out}}(\rho_{L-1/2}, n) \\ +J_n(k_b \rho_{L-1/2}) \tilde{B}_z^{\text{in}}(\rho_{L-1/2}, n) \end{Bmatrix} \end{aligned} \tag{24}$$

Equations (18), (22) and (24) indicate the procedure for calculating the total electric field $E_z(\mathbf{r})$ inside the embedding region at each iteration of the proposed MoM. Denoting $E_z^k(\rho_{L-1/2}, n)$ as the discrete version of $E_z(\mathbf{r})$ at kth iteration, the induced source $\psi_z(\rho_{L-1/2}, n) = \chi(\rho_{L-1/2}, n) E_z^k(\rho_{L-1/2}, n)$ and its FFT $\tilde{\psi}_z(\rho_{L-1/2}, n)$ are obtained. Afterward, $\tilde{A}_z(\rho_{L-1/2}, n)$ is calculated using Eqs. (18), (22) and (24) and the inverse FFT provides $A_z(\rho_{L-1/2}, n)$ and we have

$$E_z^{k+1}(\rho_{L-1/2}, n) = E_z^i(\rho_{L-1/2}, n) + k_b^2 A_z(\rho_{L-1/2}, n) \tag{25}$$

We refer to the proposed method as the 1Dfft-MoM.

The computation of $\tilde{A}_z(\rho_{L-1/2}, n)$ for the entire rings $L = 1, 2, ..., M_\rho$ and N_φ spatial frequencies, i.e. $-N_\varphi / 2 + 1 \le n \le N_\varphi / 2$, needs $M_\rho \times (7N_\varphi)$ multiplications that is due for obtaining the induced source $\psi_z(\rho_{L-1/2}, n)$ and due to the complex multiplications in Eqs. (18), (22), (24). Also, $2M_\rho N_\varphi \log_2 N_\varphi$ multiplications are needed to calculate the FFT of $\psi_z(\rho_{L-1/2}, n)$ and the inverse FFT of $\tilde{A}_z(\rho_{L-1/2}, n)$ to obtain $A_z(\rho_{L-1/2}, n)$. Thus, the total number of complex multiplications would be

$$N_{\text{1DFFT}} = 2M_\rho N_\varphi \log_2(N_\varphi) + 7M_\rho N_\varphi \tag{26}$$

for each iteration of the 1Dfft-MoM. It should be noted that obtaining $A_z(\rho_{L-1/2}, n)$ from a given total electric field inside the embedding region, i.e. from $E_z^k(\rho_{L-1/2}, n)$, is the realization of the MVP.

It is worth noting that after calculating the electric field inside the embedding region by the 2Dfft-MoM, the integral of (2) is, numerically, computed to obtain the field at any point outside the embedding region. That means the calculation of the electric field at any point $\mathbf{r}$ outside the object region needs $M_x \times N_y$ complex multiplications. However, the 1Dfft-MoM can calculate

scattering field out of the embedding region efficiently. There are M_ρ rings in radial division of polar coordination; hence, if $L = M_\rho$ in (14), we have

$$\tilde{A}_z^{\text{out}}(\rho_{M_\rho}, n) = \frac{-j\pi}{2} H_n^{(2)}(k_b \rho_{M_\rho}) \sum_{m=1}^{M_\rho} \int_{\rho_{m-1}}^{\rho_m} \rho' J_n(k_b \rho') \tilde{\psi}_z(\rho', n) d\rho' \tag{27}$$

for the last ring. Because $\tilde{\psi}_z(\rho', n)$ is zero for $\rho' > \rho_{M_\rho}$ in (27), the field for $\rho > \rho_{M_\rho}$, out of the embedding region, is given by

$$\tilde{A}_z^{\text{out}}(\rho, n) = \frac{H_n^{(2)}(k_b \rho)}{H_n^{(2)}(k_b \rho_{M_\rho})} \tilde{A}_z^{\text{out}}(\rho_{M_\rho}, n) \tag{28}$$

Using (28), the calculation of the electric field on all N_φ points on a circle outside the embedding region requires $2N_\varphi$ complex multiplications to obtain $\tilde{A}_z^{\text{out}}(\rho, n)$ and then $N_\varphi \log_2(N_\varphi)$ complex multiplications for inverse FFT of $\tilde{A}_z^{\text{out}}(\rho, n)$. Thus, the total computation would be $N_\varphi \log_2(4N_\varphi)$ and the computational cost for one point is $\log_2(4N_\varphi)$. Comparing to the 2Dfft-MoM, the computational efficiency is, considerably, improved in the calculation of the electric field outside the embedding region. This improvement is, particularly, attractive in 2D electromagnetic inverse scattering problems, where, the calculation of the field on a circle outside the object region is required at each inversion iteration [26, 27].

IV. NUMERICAL RESULTS

In this section, the scattering fields from various homogeneous and inhomogeneous dielectric cylinders will be computed to demonstrate the performance and merits of the proposed method. The results of 1Dfft-MoM are obtained for different cylinders, such as squares, circles and nonsymmetrical cylinders in different scenarios and compared with results from conventional 2Dfft-MoM and COMSOL software. The background medium in all examples is air.

To solve scattering problems, the stabilized biconjugate-gradient FFT (BCGS-FFT) [16] is used. The 2Dfft-MoM is implemented in accordance with [28] to compute vector potential $A_z(\mathbf{r})$. The iteration process of BCGS is terminated when the number of iterations exceed the maximum allowed iterations that is set to 25000, or relative residual error, *Err*, satisfies the criterion (29)

$$Err = \left\| L(\mathbf{E}_z) - \mathbf{E}_z^i \right\| / \left\| \mathbf{E}_z^i \right\| \le 10^{-4} \tag{29}$$

where $L(\mathbf{E}_z)$ is the vector calculated at different points from $L[E_z(\mathbf{r})] = E_z(\mathbf{r}) - k_b^2 A_z(\mathbf{r})$ and $\| \ \|$ denotes the L_2-norm. The incident field is a unit amplitude plane wave with *z* component, traveling in *x* direction. The figures illustrate the scattered fields, which are computed on circles outside object (embedding) region. It is assumed that permeability μ_b is that of free-space μ_0. The

discretization size, Δ, for 2Dfft-MoM in x and y directions and for 1Dfft-MoM in ρ direction for all rings at frequency f is determined with respect to

$$\Delta \le \min\left(\frac{\lambda_{\min}}{10}, \frac{\delta}{2}\right) \quad , \quad \lambda_{\min} = \frac{\lambda}{\sqrt{\varepsilon_r^{\max}}} = \frac{c/f}{\sqrt{\varepsilon_r^{\max}}} \tag{30}$$

where $\varepsilon_r^{\max}$ is the maximum relative permittivity in a cylinder, c and λ are the speed of light and the wavelength in free space and δ denotes the dimension of the smallest homogeneous part in a cylinder.

The first operating frequency is chosen f = 1200 MHz because of two reasons: 1- obtaining comparable results for the models given in [29] and 2- the electromagnetic wave could penetrate into human tissues with acceptable spatial resolution in 600-1500 MHz frequency range [30]. However, in order to investigate the behavior of the methods for higher frequencies, the simulation results are provided at 6000 MHz as well. Quantity N_φ in 1Dfft-MoM is 64 at 1200 MHz and 128 at 6000 MHz for all examples.

For a convenient comparison of the performance that is in terms of accuracy and computational efficiency, we employ two criteria : the relative error and the efficiency gain G_{eff}. The relative error of computed scattering fields of 1Dfft-MoM and 2Dfft-MoM is given by [28]

$$e = \left\| \mathbf{E}_z^{\text{exact}} - k_b^2 \mathbf{A}_z \right\| \Big/ \left\| \mathbf{E}_z^{\text{exact}} \right\| \tag{31}$$

where $\mathbf{E}_z^{\text{exact}}$ is the scattered field in form of a vector obtained at different points by COMSOL as the real data set. The second comparison criterion, G_{eff}, is obtained by combining the number of iterations, the computational complexity and the operations are needed to obtain the field outside the embedding region on a circle. The number of iterations for 1Dfft-MoM ($N_{\text{Ite}}^{\text{1D}}$) and 2Dfft-MoM ($N_{\text{Ite}}^{\text{2D}}$) algorithms may be different in terms of stopping rule (29). The efficiency gain, according to (4) and (26), is, approximately, computed from

$$G_{\text{eff}} \approx 4 N_{\text{Ite}}^{\text{2D}} M_x N_y \log_2(4 M_x N_y) \Big/ N_{\text{Ite}}^{\text{1D}} M_\rho N_\varphi \log_2(N_\varphi) \tag{32}$$

It should be noted that due to symmetric nature of the objects in Subsections A and B, the scattering fields in figures 2, 3, 4 and 5 are sketched in interval [0 180] degrees for more clarification and distinguishment between the performances of 1Dfft-MoM and 2Dfft-MoM methods.

A. HOMOGENEOUS SQUARE CYLINDERS

Sharp edges are always the matters of challenge in numerical calculations. Therefore, it is the first difficulty that the proposed method should overcome. Fig. 2a shows the resultant scattering field due to a square cylinder, whose geometry is given in the figure caption. Relation (30) suggests

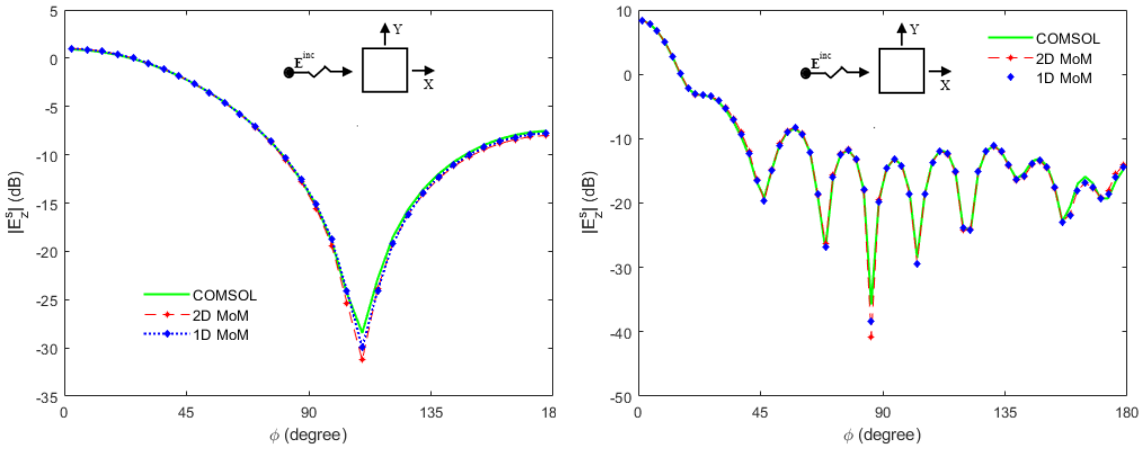

(a) (b)

Fig. 2. Computed by COMSOL, 1Dfft-MoM and 2Dfft-MoM, the scattered fields of a square cylinder at a) 1200 MHz with $\Delta_{1D} = \Delta_{2D} = 16$ mm and b) 6000 MHz with $\Delta_{1D} = 2$ mm . $\Delta_{2D} = 3$ mm. The sides of the square in x and y directions are 125 mm and it has $\varepsilon_r = 2.56$ and the fields are obtained on a circle with diameter of 375 mm

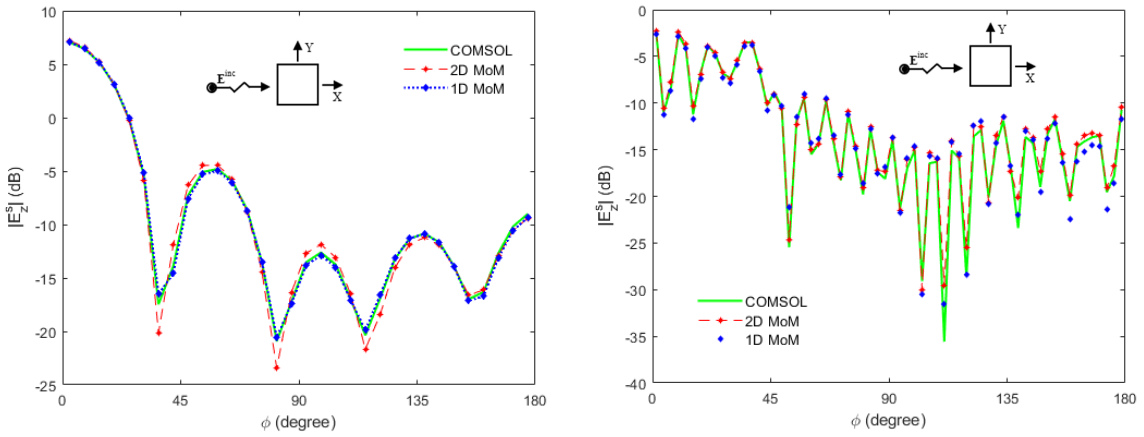

(a) (b)

Fig. 3. Illustration of the performance of 1Dfft-MoM and 2Dfft-MoM for a bigger squarecylinder at a) 1200 MHz with $\Delta_{1D} = \Delta_{2D} = 16$ mm and b) 6000 MHz with $\Delta_{1D} = 1$ mm . $\Delta_{2D} = 2$ mm. The sides of the square in x and y directions are 250 mm and the fields are obtained on a circle with diameter of 750 mm

Δ = 15.6 mm at 1200 MHz; we chose 16 mm for the discretization widths for both 1Dfft-MoM (Δ_{1D}) and for 2Dfft-MoM (Δ_{2D}) at 1200 MHz. Although it is, relatively, hard to observe, the results of 1Dfft-MoM match better to COMSOL data in Fig. 2a. In order to judge undoubtedly the performance of the both methods, we should provide the performance parameters. They are the number of cells, $N_{\text{cell}}^{1D} = M_\rho N_\varphi$ and $N_{\text{cell}}^{2D} = M_x N_y$, the relative error defined in (31), e_r^{1D} , e_r^{2D} and the efficiency gain G_{eff} for 1Dfft-MoM and 2Dfft-MoM respectively. For Fig2a, they are:

$f = 1200\,\text{MHz}$: $N_{cell}^{1D} = 448$, $N_{cell}^{2D} = 324$, $e_r^{1D} = 0.0161$, $e_r^{2D} = 0.0313$, $G_{eff} = 0.76$

The accuracy of 1Dfft-MoM is twice of that for 2Dfft-MoM; however, there is no improvement in the efficiency. This is because for relatively small objects and large Δ, the number of cells

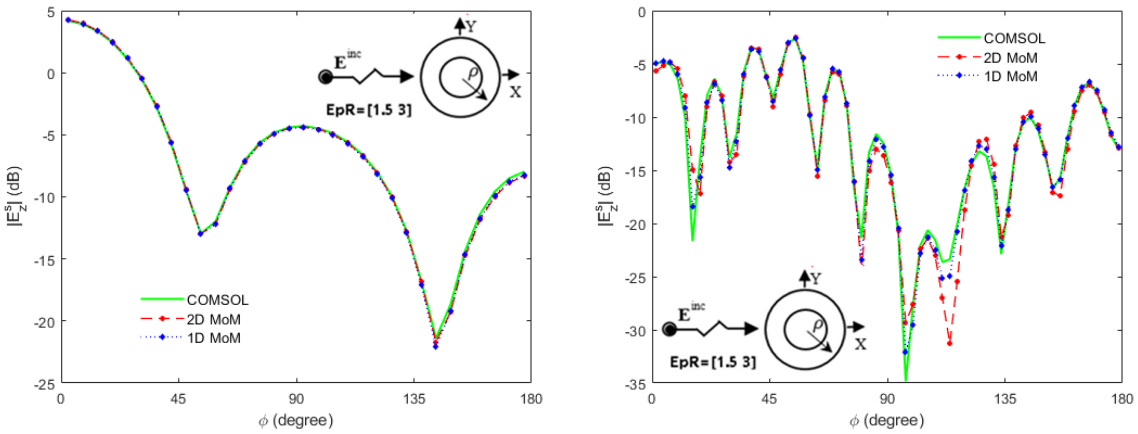

(a) (b)

Fig. 4. The scattered fields of a 2-layer cylinder at a) 1200 MHz with $\Delta_{1D} = \Delta_{2D} = 14$ mm and b) 6000 MHz with $\Delta_{1D} = 2$ mm . $\Delta_{2D} = 3$ mm. The relative permittivity and diameter of the inner cylinder are 1.5 and 100 mm and those of the outer one are 3 and 200 mm. The fields are computed on a circle with 500 mm diameter

in both x (M_x) and y (N_y) directions are reduced for 2D case, whereas M_ρ is only decreased for 1D case. Consequently, N_{cell}^{2D} is reduced more than N_{cell}^{1D} and G_{eff} is degraded with respect to (32).

For 6000 MHz, relation (30) suggests $\Delta = 3.1$ mm and hence, we set $\Delta_{1D} = 2$ mm , $\Delta_{2D} = 3$ mm and apply 1Dfft-MoM and 2Dfft-MoM for the same square cylinder. Fig. 2b illustrates the scattered fields, for which the performance parameters are:

$f = 6000\,\text{MHz}: N_{cell}^{1D} = 5888, N_{cell}^{2D} = 8100, e_r^{1D} = 0.0223, e_r^{2D} = 0.0365, G_{eff} = 1.98$

It is observed that both accuracy and efficiently of 1Dfft-MoM are improved over those of 2Dfft-MoM.

We, also, compute the scattered field for another square cylinder, whose dimensions are twice the previous one. Fig. 3 illustrates the resultant fields and the performance parameters at 1200 MHz are

$f = 1200\,\text{MHz}: N_{cell}^{1D} = 832, N_{cell}^{2D} = 1444, e_r^{1D} = 0.0200, e_r^{2D} = 0.0620, G_{eff} = 2.31$

and at 6000 MHz are

$f = 6000\,\text{MHz}: N_{cell}^{1D} = 22784, N_{cell}^{2D} = 66564, e_r^{1D} = 0.0849, e_r^{2D} = 0.0917, G_{eff} = 4.59$

Because the object is bigger making $N_{\text{cell}}^{1D} < N_{\text{cell}}^{2D}$, 1Dfft-MoM presents not only less relative error but also superior efficiency over 2Dfft-MoM. It should be noted that 1Dfft-MoM needs less storage as well.

B. TWO-LAYER CIRCULAR CYLINDERS

To further compare the two methods, we examine scattering from two circular cylinders with two

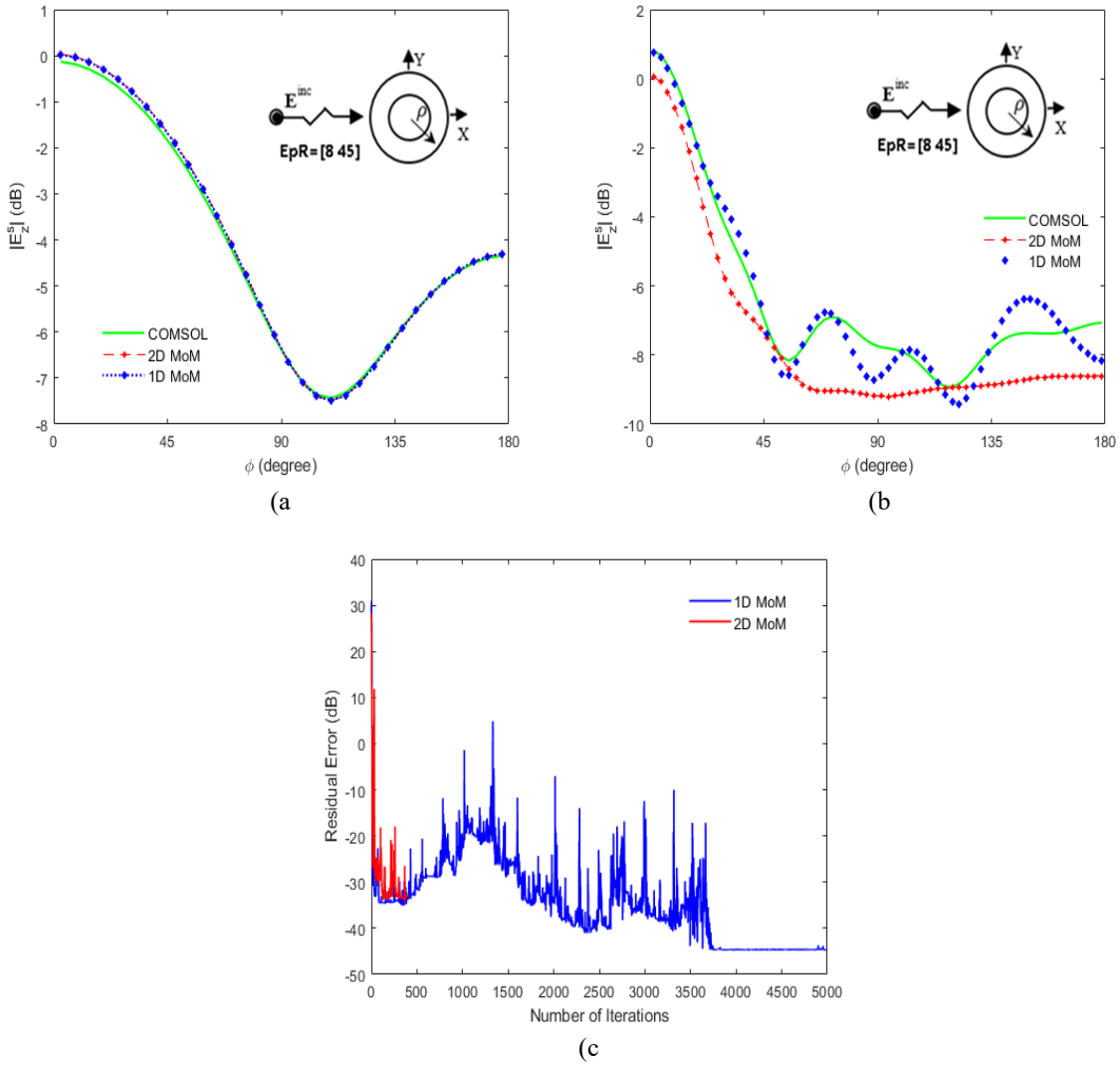

Fig. 5. Performance of 1Dfft-MoM and 2Dfft-MoM for a 2-layer cylinder with high permittivity contrast at a) 1200 MHz with $\Delta_{1D} = 2$ mm . $\Delta_{2D} = 3$ mm and b) 6000 MHz with $\Delta_{1D} = \Delta_{2D} = 0.7$ mm. Inner cylinder diameter is 25 mm with $\varepsilon_r = 8$ and that of the outer one is 75 mm with $\varepsilon_r = 45$ and the scattered fields are obtained on a circle with 225 mm diameter. c) The curve of residual error in terms of the number of iterations for 6000 MHz frequency

layers in the radial direction. The results of the first one that has relatively low permittivity contrast with the background medium (air) and large dimensions are indicated in Fig. 4. This example gives the following performance parameters:

$f = 1200\text{MHz}: N_{cell}^{1D} = 640, N_{cell}^{2D} = 1444, e_r^{1D} = 0.0162, e_r^{2D} = 0.0182, G_{eff} = 2.83$

$f = 6000\text{MHz}: N_{cell}^{1D} = 6656, N_{cell}^{2D} = 20164, e_r^{1D} = 0.0536, e_r^{2D} = 0.1218, G_{eff} = 3.00$

For this particular geometry, the 1Dfft-MoM requires less storage and computational cost. Additionally, its results agree favorably with the exact solution, while the 2Dfft-MoM solution shows some errors.

We investigate the behavior of the both methods for another 2-layer circular cylinder, having higher permittivities, i.e. $\varepsilon_r = 8$ and $\varepsilon_r = 45$ for the inner and outer cylinders respectively. Fig. 5a and Fig. 5b show the scattered fields for 1200 MHz and 6000 MHz frequencies respectively. The resultant fields of 1200 MHz fits pretty good that of COMSOL with the corresponding performance parameters as

$f = 1200\text{MHz}: N_{cell}^{1D} = 1344, N_{cell}^{2D} = 3364, e_r^{1D} = 0.0210, e_r^{2D} = 0.0238, G_{eff} = 3.44$

Nevertheless, the fitness of the scattered fields to the actual one is not satisfactory at 6000 MHz, though we set $\Delta = 0.7$ mm according to relation (30). The change of the relative residual error $Err = 45$ defined in relation (29) is depicted in Fig. 5c so as to find out whether BCGS-FFT converges. As it can be seen,

BCGS-FFT fails to converge for 2Dfft-MoM and the algorithm ends to division by zero before 500 iterations. BCGS-FFT converges for 1Dfft-MoM; but, the residual error cannot reach -80 dB, i.e. less than 10^{-4} as specified in (29). Also, BCGS-FFT behaves erratically and the residual error in some iterations is increased. Reporting in [31], such an erratic behavior is due to unsuitable selection of both initial residual error and shadow residual error that together with numerical round of error cause BCGS-FFT fails to converge. Among simple suggestion given in [31] to alleviate this pitfall is to select the intermediate solution for the scattered field with the minimum residual error in the process of BCGS-FFT algorithm. We realize this suggestion and calculate the performance parameters at the intermediate-optimum iteration. Doing so, the performance parameters for Fig. 5b are

$f = 6000\text{MHz}: N_{cell}^{1D} = 7168, N_{cell}^{2D} = 49284, e_r^{1D} = 0.0747, e_r^{2D} = 0.1573, G_{eff} = 1.04$

Microwave imaging of biological tissue is an important application of scattering from inhomogeneous objects. In light of this, we consider a simple model of a human arm shown in Fig. 6, in which the performance parameters at 1200 MHz for Fig. 6a is given by

$f = 1200\text{MHz}: N_{cell}^{1D} = 960, N_{cell}^{2D} = 529, e_r^{1D} = 0.0366, e_r^{2D} = 0.0475, G_{eff} = 2.71$

For 6000 MHz frequency, the scattered fields and the curve of residual error are shown in Fig. 6b and Fig. 6c respectively. It can be seen BCGS-FFT becomes unstable after 20000 iterations for 2Dfft-MoM.

Using outputs of the two methods at the intermediate-optimum iterations $NItr_{\text{opt}}^{1\text{D}} = 24228, NItr_{\text{opt}}^{2\text{D}} = 14934$, Fig. 6b indicates the scattered field with the performance parameters as:

$f = 6000\text{MHz}: N_{cell}^{1D} = 24320, N_{cell}^{2D} = 143641, e_r^{1D} = 0.0539, e_r^{2D} = 0.1070, G_{eff} = 27.84$

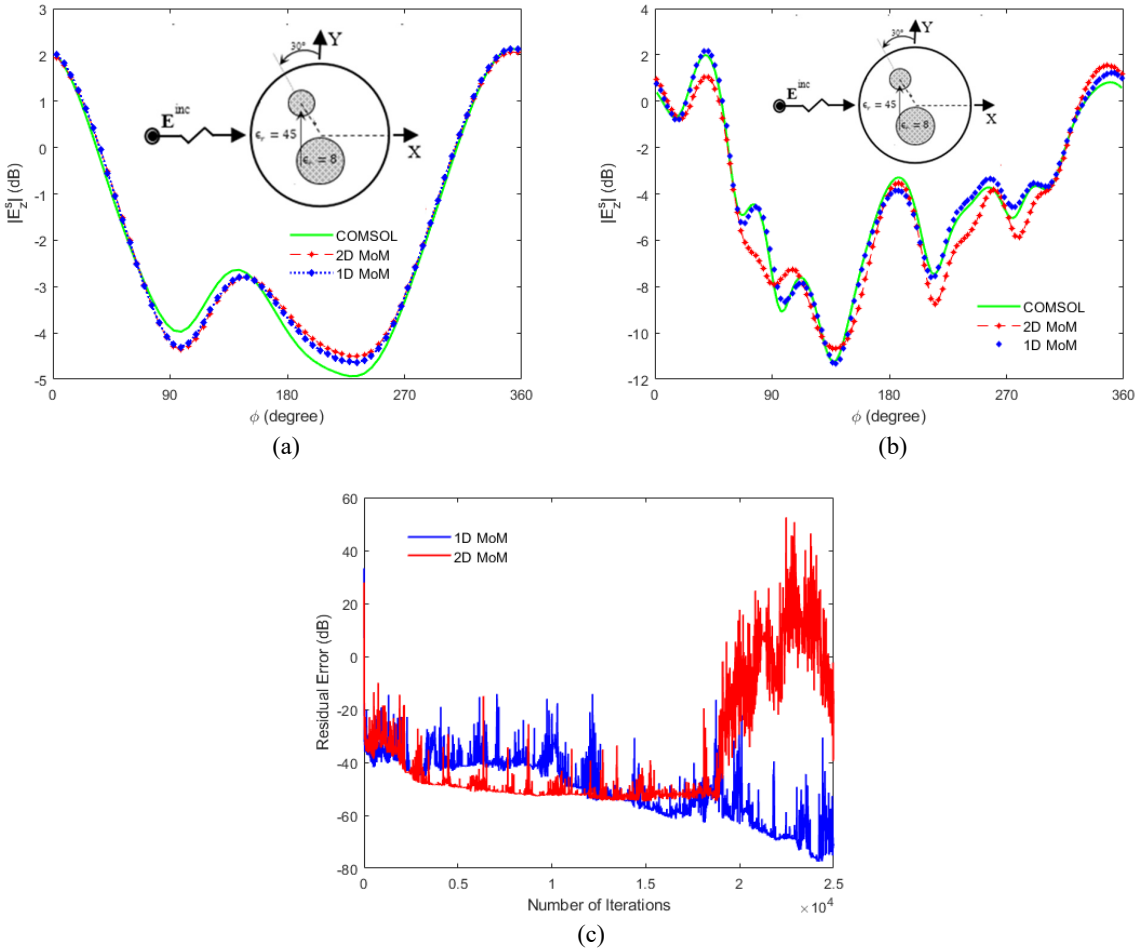

Fig. 6. The scattered fields of an arm model with $\varepsilon_r = 8$ for bones and $\varepsilon_r = 45$ for muscle at (a) 1200 MHz with $\Delta_{1D} = 3$ mm . $\Delta_{2D} = 4$ mm and (b) 6000 MHz with $\Delta_{1D} = \Delta_{2D} = 0.2$ mm. The fields are obtained on a circle with diameter of 135 mm. (c) The curve of residual error in terms of the number of iterations for 6000 MHz frequency

For this nonsymmetrical object, 1Dfft-MoM outperforms 2Dfft-MoM and presents little deviation from COMSOL data.

The quantitative parameters for Fig. 2, 3, 4, 5 and 6 are summarized in Table 1 for easy comparison. One can see that the accuracy and the computational efficiency of the 1Dfft-MoM are superior over

Returning to the comparison of 1Dfft-MoM and 2Dfft-MoM, one can conclude from Fig. 5 and the above parameters, achieved at the intermediate-optimum iterations of $NItr_{\text{opt}}^{\text{1D}} = 3774$, $NItr_{\text{opt}}^{\text{2D}} = 366$, that 1Dfft-MoM performs better.

C. ARM MODEL

2Dfft-MoM for all three structures. Specially, for a realistic model of arm, the 1Dfft-MoM meets nearly half error of 2Dfft-MoM and exhibits higher computational efficiency.

Table 1. The parameters, accuracy and efficiency of 1Dfft-MoM and 2Dfft-MoM for different examples, whose scattered fields are illustrated in the aforementioned figures

Frequency	1200 MHz ($N\varphi$ = 64)					6000 MHz ($N\varphi$ = 128)				
	Fig.2a	Fig.3a	Fig.4a	Fig.5a	Fig.6a	Fig.2b	Fig.3b	Fig.4b	Fig.5b	Fig.6b
Δ_{1D}(mm)	16	16	14	2	3	2	1	2	0.7	0.2
Δ_{2D}(mm)	16	16	14	3	4	3	2	3	0.7	0.2
$e_{\mathrm{r}}^{1\mathrm{D}}$	0.0161	0.0200	0.0162	0.0210	0.0366	0.0223	0.0849	0.0536	0.0747	0.0539
$e_{\mathrm{r}}^{2\mathrm{D}}$	0.0313	0.0620	0.0182	0.0238	0.0475	0.0365	0.0917	0.1218	0.1573	0.1070
N_{cell}^{1D}	448	832	640	1344	960	5888	22784	6656	7168	24320
N_{cell}^{2D}	324	1444	1444	3364	529	8100	66564	20164	49284	143641
G_{eff}	0.76	2.31	2.83	3.44	2.71	1.98	4.59	3.00	1.04	27.84

V. DISCUSSION AND CONCLUSION

This paper formulates 2D TM problems within the framework of the method of moment (MoM) in polar coordinates utilizing special form of Green's function. The novel formulation allows the matrix-vector product (MVP) is computed by 1-D FFT in polar MoM (1Dfft-MoM method), whereas the MVP is computed by 2-D FFT in cartesian MoM (2Dfft-MoM method). Such an approach has two advantages: 1) no need for expanding embedding region by zero padding, whereas conventional 2Dfft-MoM method needs such an expansion. This results in the reduction of memory and computational cost, while the accuracy is preserved. 2) Because the scattered field out of the object region is calculated analytically, our approach improves the efficiency in electromagnetic inverse scattering problems and microwave imaging, where the field is required to be evaluated at some measurement points outside an object under test.

The numerical examples indicate the 1Dfft-MoM enhances the accuracy, storage use and computational efficiency. In special cases when the size of scattering objects is small and comparable with the wavelength, 1Dfft-MoM needs more storage and could pose less efficiency than the 2Dfft-MoM.

We have used BCGS to solve the set of linear equations arises in MoM for both 1Dfft-MoM and 2Dfft-MoM. The number of linear equations (i.e. number of discretized cells) in electromagnetic problems gets large when the dimension of the scattering object is large relative to the shortest wavelength. Our numerical results show that BCGS can fail to converge and becomes unstable for 2D TM problems if the number of cells is large and/or some initial parameters in BCGS are chosen improper.

Authors in [31] have addressed the BCGS drawbacks (i.e. its instability and divergency)

and provided some remedies. We have employed a remedy from [31], in which the output is an intermediate solution for the scattered field with the minimum residual error in the process of BCGS-FFT algorithm. However, the best remedy suggested in [31] is to use induced dimension reduction (IDR) method instead of BCGS. The use of IDR in MoM to solve 2D TM problems together with developing MoM for 2D TE problems in polar coordinates will be left for the future work.

APPENDIX A

As $\rho \to 0$ and $n \to \infty$, the integrands of (19) and (23) become such diminutive or enormous that they are out of numerical computation range. To deal with this, asymptotic expansions can be implemented as

$$J_n(x) \approx \frac{1}{\sqrt{2\pi n}}\left(\frac{e\,x}{2n}\right)^n \quad , \quad a_n \equiv \left(\frac{e\,k_b}{2n}\right)^n \tag{A1}$$

$$H_n^{(2)}(x) = J_n(x) - jY_n(x) \approx \frac{1}{\sqrt{2\pi n}}\left[\left(\frac{ex}{2n}\right)^n + j\,2\left(\frac{ex}{2n}\right)^{-n}\right]$$

Then, the integral relations become

$$\int_{\rho_{m-1}}^{\rho_m} \rho' J_n(k_b\,\rho')\,d\rho' \approx \frac{a_n}{\sqrt{2\pi n}\,(n+2)}\left[\rho_m^{n+2} - \rho_{m-1}^{n+2}\right] \tag{A2}$$

$$\int_{\rho_{m-1}}^{\rho_m} \rho' H_n^{(2)}(k_b\,\rho')\,d\rho' \approx \frac{1}{\sqrt{2\pi n}}\left\{\begin{array}{l} \dfrac{a_n}{n+2}\left[\rho_m^{n+2} - \rho_{m-1}^{n+2}\right] \\ +j\,2\,\dfrac{a_n^{-1}}{-n+2}\left[\rho_m^{-n+2} - \rho_{m-1}^{-n+2}\right] \end{array}\right\}$$

The zeroth and first order integrands of (19), (20) and (23) can be calculated using (A3).

$$\int_{\rho_{m-1}`}^{\rho_m} G_0(k_b\,\rho')\,d\rho' = \left[\begin{array}{l} \rho'\,G_0(k_b\,\rho') \\ +\dfrac{1}{2}\pi\rho'\,\mathbf{H_0}(k_b\rho')\,G_1(k_b\rho') \\ -\dfrac{1}{2}\pi\rho'\,\mathbf{H}_1(k_b\rho')\,G_0(k_b\rho') \end{array}\right]_{\rho_{m-1}`}^{\rho_m} \tag{A3}$$

$$\int_{\rho_{m-1}`}^{\rho_m} \rho' G_0(k_b\,\rho')\,d\rho' = \frac{\rho'}{k_b}G_1(k_b\,\rho')\Big|_{\rho_{m-1}`}^{\rho_m}$$

$$\int_{\rho_{m-1}`}^{\rho_m} G_1(k_b\,\rho')\,d\rho' = -G_0(k_b\,\rho')\Big|_{\rho_{m-1}`}^{\rho_m}$$

$$\int_{\rho_{m-1}`}^{\rho_m} \rho' G_1(k_b\,\rho')\,d\rho' = \frac{1}{2k_b}\pi\rho'\left[\begin{array}{l} \mathbf{H_0}(k_b\,\rho')G_1(k_b\,\rho') \\ -\mathbf{H}_1(k_b\,\rho')G_0(k_b\,\rho') \end{array}\right]_{\rho_{m-1}`}^{\rho_m}$$

where $G_n(z) = A\,J_n(z) + B\,Y_n(z)$, for $n = 0,1$ and A, B are cte.

$A = 1$, $B = -j \;\Rightarrow\; H_n^{(2)}(k_b x) = J_n(k_b x) - jY_n(k_b x) = (-1)^n H_{-n}^{(2)}(k_b x)$

The Struve functions of the zeroth $\mathbf{H}_0$ and first $\mathbf{H}_1$ orders are given by [25]

$$\mathbf{H}_0(u)=\frac{2}{\pi}\left[u-\frac{u^3}{1^2.3^2}+\frac{u^5}{1^2.3^2.5^2}-\cdots\right] \quad , \quad \mathbf{H}_1(u)=\frac{2}{\pi}\left[\frac{u^2}{1^2.3}-\frac{u^4}{1^2.3^2.5}+\frac{u^6}{1^2.3^2.5^2.7}-\cdots\right] \tag{A4}$$

REFERENCES

[1] M.N.O. Sadiku, "*Numerical Techniques in Electromagnetics (2nd Ed.)*," Boca Radon USA: CRC Press, 2001.

[2] D.V. Davidson, "*Computational Electromagnetics for RF and Microwaves Engineering*," Cambridge: Cambridge University Press, 2005.

[3] W.C. Gibson, "*The Method of Moments in Electromagnetics*," New York: Chapman & Hall/CRC, 2008.

[4] J.M. Jin, "*The Finite Element Method in Electromagnetics (3rd Ed.)*," New Jersey: Wiley-IEEE Press, 2014.

[5] A. Taflove and S. Hagness, "*Computational Electrodynamics: The Finite-Difference Time-Domain Method (3rd Ed.)*," Boston: Artech House, 2005.

[6] J.H. Richmond, "Scattering by a dielectric cylinder of arbitrary cross section shape," *IEEE Trans. Antennas and Propagation*, vol. AP-13, pp 334-341, May 1965.

[7] J.H. Richmond, "TE-wave scattering by a dielectric cylinder of arbitrary cross-section shape," *IEEE Trans. Antennas and Propagation*, vol. AP-14, pp 460-464, July 1966.

[8] P.M. Van Den Berg, "Iterative computational techniques in scattering based upon the integrated square error criterion," *IEEE Trans Antennas and Propagation,* vol. AP-32, pp 1063-1071, Oct. 1984.

[9] T.K. Sarkar, E. Arvas, and Rao SM, "Application of the fast Fourier transform and the conjugate method for efficient solution of electromagnetic scattering from both electrically large and small conducting bodies," *Electromagnetics*, no. 5, pp 99-122, 1985.

[10] C.C. Su, "Calculation of electromagnetic scattering from a dielectric cylinder using the conjugate gradient method and FFT," *IEEE Trans Antennas and Propagation*, vol. 35, no. 12, pp 1418-1425, Dec. 1987.

[11] D.T. Borup, D.M. Sullivan, and O.P. Gandhi, "Comparison of the FFT conjugate gradient method and the finite-difference time-domain method for the 2-d absorption problem," *IEEE Trans. Microwave Theory Tech.*, vol. MTT-35, pp 383-395, April 1987.

[12] P. Zwarmborn, and P.M. Van Den Berg, "A weak form of the conjugate gradient FFT method for two-dimensional TE scattering problems," *IEEE Trans Microwave Theory and Tech.*, vol. 39, no. 6, pp 953-960, June 1991.

[13] T.J. Peters, and J.L. Volakis, "On the formulation and implementation of a conjugate gradient FFT method," *Jour. Electromagnetic Waves Appl.*, vol. 3, no. 8, pp 675-696, April 2012.

[14] Z.Q. Zhang, and Q.H. Liu, "Three-dimensional weak-form conjugate- and biconjugate-gradient FFT methods for volume integral equations, "*Microwave Opt. Tech. Lett.*, vol. 29, no. 5, pp 350-356, April 2001.

[15] H. Gan, and W.C. Chew, "A discrete BCG-FFT algorithm for solving 3D inhomogeneous scatterer problems," *Jour. Electromagnetic Waves Appl.*, vol. 9, no. 10, pp 1339-1357, April 2012.

[16] X. Xu, Q.H. Liu, and Z.W. Zhang, "The stabilized biconjugate gradient fast Fourier transform method for electromagnetic scattering," *Proceedings of International Symposium of IEEE Antennas and Propagation Society*, TX USA, June 2002.

[17] L. Zhuang, S. He, X.B. Ye, W. Hu, W. Yu, and G. Zhu, "The BCGS-FFT method combined with an improved discrete complex image method for EM scattering from electrically large objects in multilayered media," *IEEE Trans. on Geoscience and Remote Sensing*, vol. 48, no. 3, pp 1180-1185, March 2010.

[18] F. Han, J. Zhuo, N. Liu, Y. Liu, H. Liu, and Q. Liu, "Fast solution of electromagnetic scattering for 3-D inhomogeneous anisotropic objects embedded in layered uniaxial media by the BCGS-FFT method," *IEEE*

Trans. on Antennas and Propagation, vol. 67, no. 3, pp. 1748-1759, Mar. 2019.

[19] P.M. Van Den Berg, "*Forward and Inverse Scattering Algorithms Based on Contrast Source Integral Equations*," Hoboken (NJ), John Wiley & Sons, 2021.

[20] M. Parizi and M. Nakhkash, "Solution of 2-D electromagnetic problems for inhomogeneous objects using 1-D FFT," *Journal of Communication Engineering (JCE)*, vol. 9, no. 1, pp. 109-125, June 2020.

[21] N. Chamanara, "A new integral equation formulation for scattering of electromagnetic waves by 2D conducting structures using cylindrical harmonics," *Progress in Electromagnetics Research M*, vol. 7, pp 165-177, 2009.

[22] R. Guo, T. Shan, X. Song, and et al., "Physics embedded deep neural network for solving volume integral equation: 2-D case," *IEEE Trans Antennas and Propagation*, vol. 70, no. 8, pp 6135-6147, August 2022.

[23] M.F. Catedra, R.F. Torres, J. Basterrechea, and et al, "*The CG-FFT Method: Application of Signal Processing Techniques to Electromagnetics*," Bostion, Artech House, 1995.

[24] J. Harrington, "*Time Harmonic Electromagnetic Fields*," USA, Wiley-IEEE Press, 2001.

[25] M. Abramowitz, and I. A. Stegam, "*Handbook of Mathematical Functions*," NY Dover, Cambridge Univ Press, 1965.

[26] N. Ghavami, P.P. Smith, G. Tiberi, and et al, "Non-iterative beamforming based on Huy-gens principle for multistatic ultrawide band radar: application to breast imaging," *IET Microwaves, Antennas & Propagation*, vol. 9, no. 12, pp 1233-1240, Sept. 2015.

[27] A. Zakaria, and J. LoVetri, "The finite-element method contrast source inversion algorithm for 2D transverse electric vectorial problems," *IEEE Trans Antennas and Propagation*, vol. 60, no. 10, pp 4757-4765, Oct. 2012.

[28] P. Mojabi, "*Investigation and development of algorithms and techniques for microwave tomography*," Ph.D. dissertation, University of Manitoba, May 2010.

[29] M. A. Jensen, and J. D. Freeze, "A recursive Green's function method for boundary integral analysis of inhomogeneous domains," *IEEE Trans. on Antennas and Propagation*, vol. 46, no. 12, pp. 1810–1816, Dec. 1998.

[30] R. Scapaticci, L. Di Donato, I. Catapano, and L. Crocco, "A feasibility study on microwave imaging for brain stroke monitoring," *Progress in Electromagnetics Research*, vol. 40, pp. 305–324, May 2012.

[31] C. Schoutrop, J. T. Boonkkamp, and J. V. Dijk, "Reliability investigation of BiCGStab and IDR solvers for the advection-diffusion-reaction equation," *Communication in Computational Physics*, vol. 32, No. 1, pp. 156-188, July 2022.